Dalton Transactions

ROYAL SOCIETY OF CHEMISTRY

PAPER

View Article Online
View Journal | View Issue

Cite this: *Dalton Trans.*, 2026, **55**, 735

Fluorine-substituted cyclometallated rhodium(III) complexes with α-diimine ancillary ligands: synthesis, structure, and photophysical and DNA-binding properties

Patryk Wójcik, [a] Camille Latouche, *[b,c] Kinga Suwińska, [d] Anna Kamecka, *[a] Joanna Masternak [e] and Mariusz Urbaniak[e]

Received 3rd October 2025,
Accepted 2nd December 2025

DOI: 10.1039/d5dt02369f

rsc.li/dalton

A series of cationic $[Rh(dfppz)_2(N^N)]^+$ complexes, incorporating cyclometallating 1-(2,4-difluorophenyl)-1*H*-pyrazolato and α-diimine ligands [2,2′-bipyridine, 1,10-phenanthroline and their derivatives], were synthesized as PF_6^- salts *via* cleavage of the μ-dichloro-bridged dimer $[(dfppz)_2Rh\text{-}\mu\text{-}Cl]_2$ with the respective N^N ligands. The complexes were fully characterized by NMR spectroscopy, electrospray ionization mass spectrometry, and single-crystal X-ray diffraction. Time-dependent DFT (TDDFT) studies were performed to gain insight into their electronic structures. At 77 K in 1 : 1 MeOH/EtOH glass matrices, the complexes exhibit intense luminescence, whereas in MeCN at ambient temperature, they are weakly emissive or non-emissive. Their photophysical behavior was systematically compared with that of non-fluorinated $[Rh(ppz)_2(N^N)]^+$ analogues to evaluate the impact of fluorination on the emission properties. Preliminary DNA-binding studies were also conducted using emission titrations.

Introduction

Rhodium(III) complexes are being increasingly explored in diverse fields, particularly as catalysts in organic synthesis[1] and as potential anticancer agents in biomedicine.[2–7] Since DNA remains a primary target for many anticancer drugs, numerous studies have been carried out to investigate the interactions of Rh(III) complexes with different DNA sequences to elucidate their mechanisms of action.[8–14] The binding mode and affinity depend strongly on the ligand structure, charge, and steric properties of the complex. Studies have shown that the greatest intercalation ability is demonstrated by complexes containing α-diimine ligands, such as 1,10-phenanthroline, 2,2′-bipyridine, and their derivatives with fused rings.[8,10,15–17]

Owing to their isoelectronic configuration with Ir(III) and Pt(IV) ions, Rh(III) complexes serve as valuable analogues for exploring how subtle electronic and structural modifications influence their photophysical properties and the nature of the excited state. In contrast to Ir(III) complexes, renowned for their strong phosphorescence,[18] Rh(III) analogues typically exhibit low luminescence efficiency at room temperature.[19]

According to the literature, heteroleptic Rh(III) complexes of the $[Rh(C^N)_2(N^N)]^+$ type, where C^N denotes a cyclometallating ligand and N^N an ancillary α-diimine ligand, are generally weakly emissive, with quantum yield values not exceeding a few percent,[4,20,21] or non-emissive at room temperature.[4,10,20,22–29] The emission lifetime can be very short when the emission originates from a singlet excited state, as in the case of most $[Rh(C^N)_2(dppz)]^+$ complexes,[10] or falls within the microsecond range when it arises predominantly from a triplet excited state (ILCT), with some mixing of MLCT $d\pi(Rh) \rightarrow \pi^*(C^N)$ character.[20,21] In a glass matrix at 77 K, the emission spectra of Rh(III) complexes exhibit a well-resolved vibrational structure, and the emission lifetimes at this temperature are long, reaching up to several milliseconds.[20,23,25–27] Recent studies employing high-throughput synthesis and screening (HTSS) methods have shown that the luminescence properties of Rh(III) complexes are largely controlled by the identity of the ancillary diimine ligand and can be modulated through rational ligand design.[19]

Fluorination of ligands is known to significantly affect both the photophysical[30–32] and biomedical[33,34] properties of cyclometallated complexes. The introduction of fluorine atoms into aromatic or heteroaromatic frameworks can markedly influ-

[a]*University of Siedlce, Faculty of Natural Sciences, 3 Maja 54, 08-110 Siedlce, Poland. E-mail: anna.kamecka@uws.edu.pl*
[b]*Nantes Université, CNRS, Institut des Matériaux de Nantes Jean Rouxel, IMN, F-44000 Nantes, France. E-mail: Camille.Latouche@cnrs-imn.fr*
[c]*Institut Universitaire de France, Paris 75005, France*
[d]*Cardinal Stefan Wyszyński University in Warsaw, Faculty of Mathematics and Natural Sciences, K. Wóycickiego 1/3, 01-938 Warszawa, Poland*
[e]*Jan Kochanowski University of Kielce, Faculty of Natural Sciences, Uniwersytecka 7, 25-406 Kielce, Poland*

ence metal–ligand bonding, redox potential, and the relative energies of charge-transfer states. In particular, fluorinated cyclometallating ligands have been shown to modulate both emissive properties and chemical stability in a variety of Ir(III) and Pt(II/IV) systems, highlighting fluorine's ability to fine-tune excited-state energies and deactivation pathways.[30–32,34] Despite these advances, systematic studies on fluorinated Rh(III) complexes remain limited, leaving an incomplete understanding of how such electronic modifications affect the photophysical behaviour of these isoelectronic systems.

Herein, we report a new series of cationic $[Rh(C^N)_2(N^N)]^+$ complexes employing C-deprotonated 1-(2,4-difluorophenyl)-1*H*-pyrazole ($dfppz^-$) as a cyclometallating ligand and a set of α-diimine (N^N) ligands with varying electron-acceptor strengths as ancillary ligands (Scheme 1a). Our recent work has focused on cyclometallated complexes of the $[M(C^N)_2(N^N)]^{+/2+}$ type with α-diamine ligands, in which the central metal ion was Ir(III),[35,36] and its isoelectronic ions are Rh(III)[37] and Pt(IV) (Scheme 1b).[38] The photoluminescence properties of these analogous series of complexes, which share very similar geometries and other structural features, have been thoroughly investigated and compared. Despite their structural similarity, these complexes exhibit markedly different emission behaviours at both 298 K and at 77 K. Whereas Ir(III) derivatives are strongly luminescent, their Rh(III) and Pt(IV) analogues are weakly emissive or non-emissive at room temperature. In the case of $[Rh(ppz)_2(N^N)]^+$ complexes (Hppz = 1-phenyl-1*H*-pyrazole), the emission quenching at 298 K has been explained by the presence of a thermally activated deactivation channel associated with a low-lying triplet metal-centered (^{3*}MC) state.[37] In contrast, for the Pt(IV) derivatives, nonradiative deactivation at this temperature has been attributed to the population of a ligand-to-metal charge transfer (LMCT) state.[38]

We further compared the spectroscopic and photophysical properties of these new $[Rh(dfppz)_2(N^N)]^+$ complexes with those of non-fluorinated Rh(III) analogues. Our systematic approach aims to elucidate how fluorine substitution influences the spectroscopic and photophysical properties of Rh(III) complexes. In addition to the spectroscopic and photophysical characterization, we also examined the DNA-binding properties of these fluorinated Rh(III) complexes, providing complementary insight into their potential bioactivity.

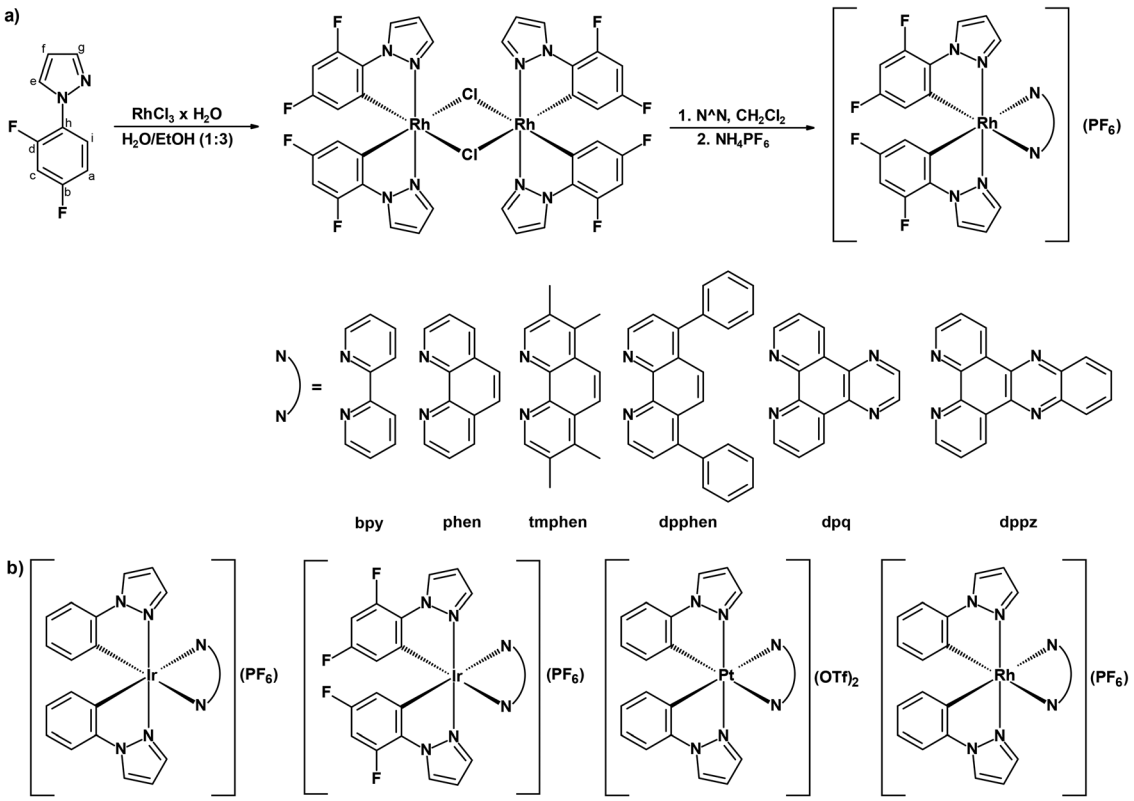

Scheme 1 (a) Synthetic routes for the preparation of the $[Rh(dfppz)_2(N^N)](PF_6)$ complexes and the chemical structures of the C^N and N^N ligands used in this study: 1-(2,4-difluorophenyl)-1*H*-pyrazole – Hdfppz; 2,2′-bipyridine – bpy; 1,10-phenanthroline – phen; 3,4,7,8-tetramethyl-1,10-phenanthroline – tmphen; 4,7-diphenyl-1,10-phenathroline – dpphen; dipyrido[3,2-*a*:2′,3′-*f*]-quinoxaline – dpq; and dipyrido[3,2-*a*:2′,3′-*c*] phenazine – dppz. The numbering of the received complexes is as follows: $[Rh(dfppz)_2(bpy)](PF_6)$ – **Rh1**; $[Rh(dfppz)_2(phen)](PF_6)$ – **Rh2**; $[Rh(dfppz)_2(tmphen)](PF_6)$ – **Rh3**; $[Rh(dfppz)_2(dpphen)](PF_6)$ – **Rh4**; $[Rh(dfppz)_2(dpq)](PF_6)$ – **Rh5**; and $[Rh(dfppz)_2(dppz)](PF_6)$ – **Rh6**. (b) Chemical structures of previously studied series of complexes: $[Ir(ppz)_2(N^N)](PF_6)$, $[Ir(dfppz)_2(N^N)](PF_6)$, $[Pt(ppz)_2(N^N)](OTf)_2$ and $[Rh(ppz)_2(N^N)](PF_6)$.

Results and discussion

Synthesis and structure of cyclometallated [Rh(dfppz)$_2$(N^N)](PF$_6$) compounds

The synthetic routes and structures of the ligands are shown in Scheme 1a. The [Rh(dfppz)$_2$(N^N)](PF$_6$) complexes were prepared in two steps. First, the μ-dichloro-bridged dimer, [(dfppz)$_2$Rh-μ-Cl]$_2$, was synthesized following a literature procedure.[39–41] In the second step, the heteroleptic complexes [Rh(dfppz)$_2$(N^N)](PF$_6$) were obtained *via* cleavage of the dimer with N^N ligands, followed by anion exchange ($Cl^- \rightarrow PF_6^-$). The complexes were isolated in high yields, and their structures were confirmed by ^{1}H, ^{13}C, ^{19}F and ^{31}P NMR spectroscopy (Fig. 1 and Fig. S1–S6). Their ESI mass spectra in CH_3CN displayed the expected molecular ions (Fig. S7). The spectroscopic data are consistent with the proposed structures of the complexes.

The ^{1}H NMR spectra of [Rh(dfppz)$_2$(N^N)]$^+$ closely resemble those reported for the corresponding [Rh(ppz)$_2$(N^N)]$^+$ analogues,[37] consistent with pseudo C_2 symmetry and similar ligand arrangement. The two cyclometallating dfppz$^-$ ligands are magnetically equivalent, giving a single set of proton signals (five, as labelled in Fig. 1a), whose integrated intensities correspond to the expected ten protons of both dfppz$^-$ ligands. Comparison with non-fluorinated analogues reveals significant differences. As expected, the phenyl proton signals H$_b$ and H$_d$, corresponding to fluorine-substituted positions, are absent in the spectra of [Rh(dfppz)$_2$(N^N)]$^+$ cations. Furthermore, the signals of H$_a$ and H$_c$ protons, attached to the dfppz$^-$ carbon atoms adjacent to the fluorine-substituted carbons (δ ~5.8–5.9 ppm and 6.9 ppm, respectively), are shifted upfield relative to the corresponding signals in the spectra of [Rh(ppz)$_2$(N^N)]$^+$ (δ ~6.3–6.4 ppm and 7.2 ppm, respectively),[37] with $\Delta\delta = \delta_{[Rh(dfppz)_2(N^N)]^+} - \delta_{[Rh(ppz)_2(N^N)]^+} \approx -0.3$ and −0.5 ppm, respectively (Fig. 1a). A similar fluorine-induced effect was also observed in the spectra of the uncoordinated Hdfppz and Hppz ligands.[42]

The remaining aromatic signals in the ^{1}H NMR spectra correspond well to the coordinated N^N ligands. Their numbers, relative intensities, and splitting patterns indicate equivalence of the two halves of the N^N ligands, with all resonances showing the expected multiplicities and *J*-coupling constants. These results are fully consistent with the proposed C_2 symmetric structures of the [Rh(dfppz)$_2$(N^N)]$^+$ complexes.

The ^{13}C{^{1}H} NMR spectra of all investigated complexes show the expected number of signals corresponding to the symmetry-related carbon atoms of the coordinated ligands (Fig. 1b and Fig. S1–S6). A distinctive feature of these spectra is the presence of ^{13}C–^{19}F couplings to the aromatic carbons. In particular, signals at $\delta \approx 150$ and 160 ppm exhibit large coupling constants ($J_{C-F} \approx 251$ and 254 Hz), confirming the presence of fluorine substituents. These resonances are shifted downfield relative to the corresponding signals in the spectra of [Rh(ppz)$_2$(N^N)]$^+$ (Fig. 1b).[37] Similar to the complexes containing ppz$^-$ cyclometallating ligands, a characteristic doublet at $\delta \approx 153$–154 ppm with $J_{C-Rh} \approx 31$ Hz confirms

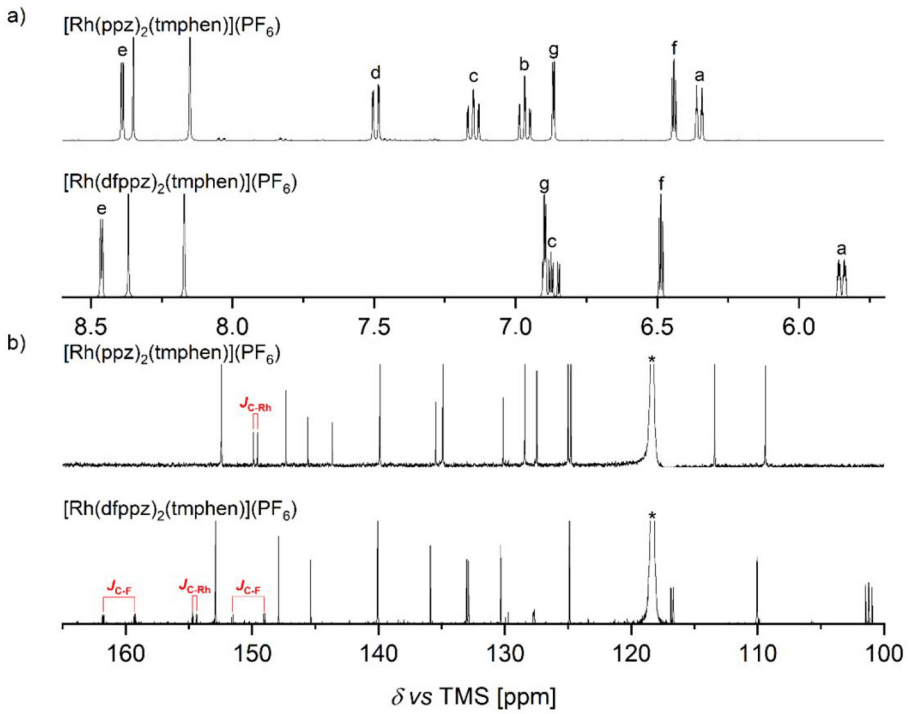

Fig. 1 ^{1}H NMR spectra (a) and ^{13}C NMR spectra (b) of the [Rh(ppz)$_2$(tmphen)]$^+$ and [Rh(dfppz)$_2$(tmphen)]$^+$ complexes in CD_3CN solution. The letters a–g indicate the signals assigned to the protons of the ppz$^-$ or dfppz$^-$ ligand, respectively. The asterisk * indicates the signal assigned to acetonitrile.

the cyclometallation of the Rh(III) ion. In the [Rh(dfppz)$_2$(N^N)]$^+$ spectra, however, this signal is shifted several ppm downfield compared to the non-fluorinated analogues.

In the ^{19}F NMR spectra of the studied complexes, three well-resolved resonances are observed. The signal at approximately −73 ppm, characterized by a typical coupling constant (~706–707 Hz), is attributed to the PF_6^- counterion. The remaining two fluorine resonances, detected at −113.5 to −113.8 ppm and −123.6 to −123.8 ppm, are assigned to the fluorine substituents of the cyclometallating dfppz$^-$ ligands. The chemical shift values are in good agreement with those reported for structurally related fluorinated ligands,[43] thereby supporting the proposed coordination in the complexes. These findings are further supported by the ^{31}P NMR spectra. All investigated [Rh(dfppz)$_2$(N^N)](PF_6) complexes display very similar features with a characteristic septet at $\delta \approx -144.7$ ppm with $J_{P-F} \approx 706–707$ Hz, corresponding to the PF_6^- counter anion.

Single-crystal X-ray diffraction analyses were performed for selected [Rh(dfppz)$_2$(N^N)]$^+$ complexes. Perspective views of the molecular structures are shown in Fig. 2 and selected bond distances are summarized in Table 1. These complexes exhibit the expected octahedral coordination geometry, with two dfppz-chelating ligands occupying four coordination sites and the N^N-chelating ligand occupying the remaining two coordination positions. The *trans* bond angles at the rhodium center (N_{dfppz}–Rh–N_{dfppz} and N_{N^N}–Rh–C_{dfppz}) fall within the range of 170.7–174.3°, indicating only minor deviations from an ideal octahedral geometry. Similarly, with respect to the related [Rh(ppz)$_2$(N^N)]$^+$ complexes, the pyrazole nitrogen atoms of the cyclometallating dfppz ligands adopt a mutual *trans* arrangement, while the Rh–C_{dfppz} bonds are oriented *cis* to one another. The Rh–N_{N^N} bond lengths (~2.14–2.16 Å) are significantly longer than the Rh–N_{dfppz} bond lengths (~2.01–2.03 Å), consistent with the *trans*-influence of the cyclometallating carbon atoms.[44] Comparable bond-length differences have been reported for other cyclometallated rhodium(III) polypyridine complexes.[10,20,29] Comparison of [Rh(dfppz)$_2$(N^N)]$^+$ with the analogous [Rh(ppz)$_2$(N^N)]$^+$ complexes reveals only subtle structural differences, with the Rh–N_{N^N} bonds in the dfppz derivatives being shorter by approximately 0.01 or 0.02 Å.[37]

As shown in Fig. S8–S12 (*cf.* the SI), apart from obvious electrostatic interactions, significant numbers of weak C–H···F hydrogen bonds between [Rh(dfppz)$_2$(N^N)]$^+$ complex cations and PF_6^- anions are present in the crystal structures. In the structure of the [Rh(dfppz)$_2$(bpy)](PF_6) complex, PF_6^- anions are located in the cavities formed between the neighboring complex cations (Fig. S8).

There are two symmetry-independent cation complexes and PF_6^- anions in the unit cell of [Rh(dfppz)$_2$(phen)](PF_6). Each symmetry-independent cation forms homo-molecular centrosymmetric dimers of A–A or B–B type *via* π–π interactions between dfppz ligands. The dimers are further arranged along the [011] crystallographic direction into columns of the type ···–A–A–B–B–A–A–B–B–··· *via* π–π interactions between phen ligands. Finally, columns of cations are arranged in layers that are separated by layers of anions. The layers are parallel to the *bc* crystallographic plane. Solvent molecules are located in the complex cation layer between the cations (Fig. S9). The [Rh(dfppz)$_2$(dpphen)](PF_6) compound crystallizes with one chlorobenzene molecule per molecule of salt. Complex cations form infinite ribbons *via* multiple C–H···π interactions between dfppz and dpphen ligands along the [10$\bar{1}$] crystallographic direction. Ribbons are arranged in such a way that the dpphen ligands penetrate the interlayer space forming channels filled with alternately arranged PF_6^- anions and C_6H_5Cl solvent molecules connected by weak C–H···F interactions (Fig. S10). The [Rh(dfppz)$_2$(dpq)](PF_6) and [Rh(dfppz)$_2$(dppz)](PF_6) crystals are isostructural. The **Rh5** and **Rh6** complex cations are arranged in columns along the *c* crystallographic axis *via* π–π stacking interactions between the dpq or dppz ligands. Additionally, between the dfppz ligands of neighboring columns of **Rh5** cations, π–π and C–H···π interactions occur and PF_6^- anions are located in the cavities formed between the cation columns. These cavities are interconnected by small (unoccupied) cavities to form irregular channels that are parallel to the columns (Fig. S11). In turn, PF_6^- anions in the **Rh6** structure are located in the channels formed between the cation columns and are parallel to the columns (Fig. S12). The lack of π–π and C–H···π interactions between the dfppz ligands of adjacent cation columns in the case of this complex is due to the size difference between these two ligands.

The structures of the investigated complexes were optimized using the DFT/B3PW91 functional, and the resulting bond lengths are summarized in Table 1. The calculated values reproduce the X-ray crystal structures well, with deviations of only 0.01–0.05 Å in the S_0 geometries. Slightly longer Rh–N_{N^N} bond lengths are observed but generally do not exceed 0.1 Å, which is typical for such complexes. Overall, the good agreement between the computed and experimental data validates the computational protocol for investigating the optoelectronic properties.

Electronic absorption spectra

UV-vis absorption spectra of [Rh(dfppz)$_2$(N^N)](PF_6) complexes were recorded in acetonitrile solution (c = 0.16 mM) at 298 K. The absorption maxima of all Rh(III) complexes are summarized in Table 2, and the corresponding spectra of these complexes are shown in Fig. S13 (*cf.* the SI). The electronic absorption spectra display intense high-energy bands and shoulders between 200 and 310 nm as well as weaker, lower-energy absorption signals in the lower-energy bands of rather low intensity in the 330–380 nm region. With reference to previous studies on the [(dfppz)$_2$Rh-μ-Cl]$_2$ precursor[41] and related Rh(III) complexes,[28,29,37] the high-energy bands and shoulders (with maximum molar absorption coefficients ε in the order of 10^4 M^{-1} cm^{-1}) are attributed to the ^{1}IL ($\pi \rightarrow \pi^*$) transitions of the diimine and dfppz$^-$ ligands. In the lower energy region, the weaker absorption bands (ε in the order of several thousand M^{-1} cm^{-1}), absent in the spectra of the free Hdfppz and N^N ligands and in the [(dfppz)$_2$Rh-μ-Cl]$_2$ precursor, are assigned to spin-allowed ^{1}MLCT (d_π(Rh) → π*(diimine and

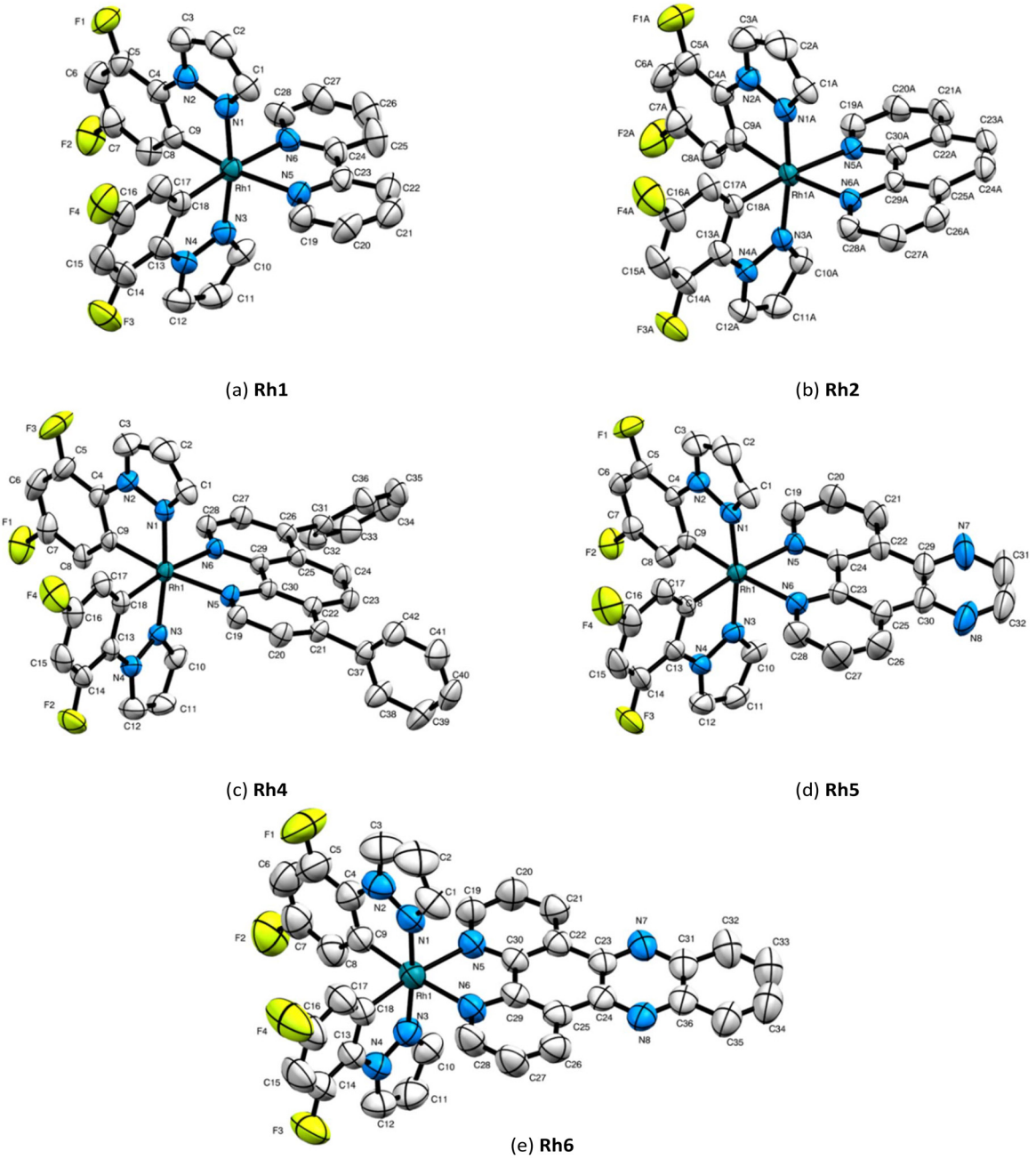

Fig. 2 Molecular structures of the complexes $[Rh(dfppz)_2(bpy)]^+$ (a), $[Rh(dfppz)_2(phen)]^+$ (b), $[Rh(ppz)_2(dpphen)]^+$ (c), $[Rh(ppz)_2(dpq)]^+$ (d), and $[Rh(ppz)_2(dppz)]^+$ (e) with atomic labelling and displacement ellipsoids drawn at the 50% probability level. Hydrogen atoms have been omitted for clarity.

dfppz$^-$)) transitions. The lowest-energy bands of the $[Rh(dfppz)_2(N^N)](PF_6)$ series are located at slightly different wavelengths, depending on the electron-withdrawing properties of the coordinated N^N ligand (Table 2). The exception is $[Rh(ppz)_2(dppz)](PF_6)$, where the extensive π-aromatic system leads to overlap of MLCT and ligand-centered (LC) transitions. A comparison of the absorption spectra of the investigated $[Rh(dfppz)_2(N^N)](PF_6)$ complexes with their non-fluorinated analogues ($[Rh(ppz)_2(N^N)](PF_6)$) reveals very similar absorption profiles, with the principal distinction being a modest hypsochromic shift of the highest-energy bands in the fluorinated complexes (Fig. S13).

For more detailed information, DFT and TDDFT calculations were carried out on the investigated $[Rh(dfppz)_2(N^N)]^+$ complexes at the optimized ground state geometries in the presence of CH_2Cl_2 solvent. The HOMO and LUMO for these complexes are shown in Fig. S18–S23 (*cf.* the SI). The computation results point to the presence of a series of singlet and

Table 1 Selected metal–ligand bond lengths (Å) in the S_0 and T_0 states for the investigated $[Rh(dfppz)_2(N\hat{}N)]^+$ complexes. Data from DFT computations and X-ray investigations

	Metal–ligand bond lengths								
	CH_2Cl_2 solution, S_0			CH_2Cl_2 solution, T_0			X-ray data		
Complex	Rh–C_{dfppz}	Rh–N_{dfppz}	Rh–$N_{N\hat{}N}$	Rh–C_{dfppz}	Rh–N_{dfppz}	Rh–$N_{N\hat{}N}$	Rh–C_{dfppz}	Rh–N_{dfppz}	Rh–$N_{N\hat{}N}$
Rh1	2.000	2.030	2.176	2.002	2.030	2.159	1.996(6)	2.015(5)	2.148(4)
	2.000	2.030	2.175	2.002	2.030	2.159	2.002(6)	2.014(5)	2.137(5)
Rh2	1.998	2.030	2.168	1.999	2.029	2.182	2.005(5)	2.015(4)	2.142(4)[a]
	1.998	2.030	2.168	1.999	2.029	2.182	2.002(4)	2.003(4)	2.137(3)
Rh3	1.999	2.032	2.179	2.000	2.032	2.178			
	1.999	2.032	2.179	2.000	2.032	2.178			
Rh4	1.999	2.030	2.173	1.999	2.029	2.138	2.004(3)	2.015(3)	2.138(2)
	1.999	2.030	2.173	2.007	2.032	2.178	2.014(3)	2.019(3)	2.142(2)
Rh5	1.998	2.028	2.183	1.976	2.029	2.162	2.004(3)	2.031(3)	2.137(3)
	1.998	2.028	2.183	1.976	2.029	2.162	2.008(3)	2.008(3)	2.161(3)
Rh6	1.997	2.029	2.181	1.999	2.029	2.138	2.002(5)	2.017(4)	2.151(3)
	1.997	2.029	2.181	2.007	2.032	2.176	1.999(4)	2.016(4)	2.143(4)

[a] In the case of the $[Rh(dfppz)_2(phen)]^+$ complex, there are two complex molecules with slightly different bond lengths in the unit cell. The second set of bond lengths is as follows: Rh–C_{dfppz}: 2.005(4) Å, Rh–C_{dfppz}: 2.007(4) Å, Rh–N_{dfppz}: 2.014(4) Å, Rh–N_{dfppz}: 2.013(4) Å, Rh–$N_{N\hat{}N}$: 2.142 (4) Å, and Rh–$N_{N\hat{}N}$: 2.146(3) Å.

Table 2 Absorption maxima and molar extinction coefficients in acetonitrile solution and emission properties (position of emission maxima (λ_{em}) and emission lifetimes (τ_{em})) of the investigated $[Rh(dfppz)_2(N\hat{}N)](PF_6)$ complexes; data at 77 K in MeOH/EtOH 1 : 1 glass

		77 K	
Complex	298 K λ_{abs}/nm ($\varepsilon_{max}/10^4$ M^{-1} cm^{-1})	λ_{em}/nm	τ_{em}/μs
Rh1	223.5 (5.1), 245 (3.4), 296.5 (1.9), 307 (1.8)	438, 469, 494, 504, 533	671
Rh2	226.5 (6.4), 270 (4.2), 289sh (1.7), 331 (0.17), 348 (0.13)	449, 480, 516, 556	19 100
Rh3	209 (7.2), 224 (5.8), 276 (5.2), 303sh (1.6), 334 (0.27), 351 (0.10)	462, 495,532, 576	40 000
Rh4	223 (7.5), 283 (5.6), 309sh (2.3), 341sh (0.57), 360 (0.35)	477, 512, 550, 596	11 000
Rh5	222 (5.5), 256 (7.0), 282sh (2.9), 326 (0.56), 342 (0.50)	421, 450, 482, 517sh, 548sh	395
Rh6[a]	220sh (5.9), 275 (8.4), 359 (1.3), 377 (1.5)	541, 586, 638, 699sh	158 000

[a] Room-temperature data in deoxygenated acetonitrile solution: λ_{em} = 557, 601, and 649sh nm; ϕ_{em} = 0.21%.

triplet transitions in the low-energy part of the UV-vis absorption spectra following vertical photoexcitation of the S_0 state. In all complexes, the HOMO is distributed across the metal center and the cyclometallating $dfppz^-$ ligands. The LUMO is essentially a $\pi^\star$ orbital localized on the N^N amine ligand. Thus, the lowest energy $S_0 \rightarrow S_1$ transitions of the discussed complexes involve the HOMO and LUMO and can be assigned mainly to the MLL′CT transition between $[Rh(dfppz)_2]^+$ and the electron acceptor N^N ligand.

Emission properties

All studied $[Rh(dfppz)_2(N\hat{}N)]^+$ complexes are emissive in MeOH/EtOH (1 : 1, v/v) glass at 77 K (Table 2). These complexes display highly structured emission bands with pronounced vibrational progression (Fig. S14) and monoexponential decay with very long emission lifetimes (several hundred microseconds or even several dozen milliseconds, Table 2), which have been observed for other Rh(III) complexes.[25,27,37] The emission bands of these complexes are shifted with respect to one another and appear in a wavelength region distinct from that of the emission band of the free pyrazole ligand. Furthermore, these spectra are almost identical in energy and shape with those previously reported for $[Rh(ppz)_2(N\hat{}N)]^+$ analogues, containing non-fluorinated cyclometallating ligands,[37] or free N^N ligands (Fig. S14).[24,27,45,46] Therefore, it can be assumed that the emitting state has a well-pronounced ^{3}*LC character localized mainly on the coordinated N^N ligand in these heteroleptic complexes. The cyclometallating $dfppz^-$ ligands do not contribute to the emission at 77 K, because the ^{3}*LC(dfppz) state lies at higher energy than the emitting ^{3}*LC (N^N) states (Fig. S15). The results show that the substitution of fluorine substituents in the cyclometallating ligands results in a significant prolongation of the phosphorescence lifetime compared to their non-fluorinated analogues. A similar effect was observed in the case of cyclometallated Ir(III) complexes.[30,36]

To gain deeper insight into the emission properties of the studied $[Rh(dfppz)_2(N\hat{}N)]^+$ complexes, DFT computations were performed on the lowest triplet state (T_0) luminescence energies and corresponding spin densities (Fig. S17). The simulated emission spectra obtained using a state-of-the art method (adiabatic Hessian) match nicely with experimental

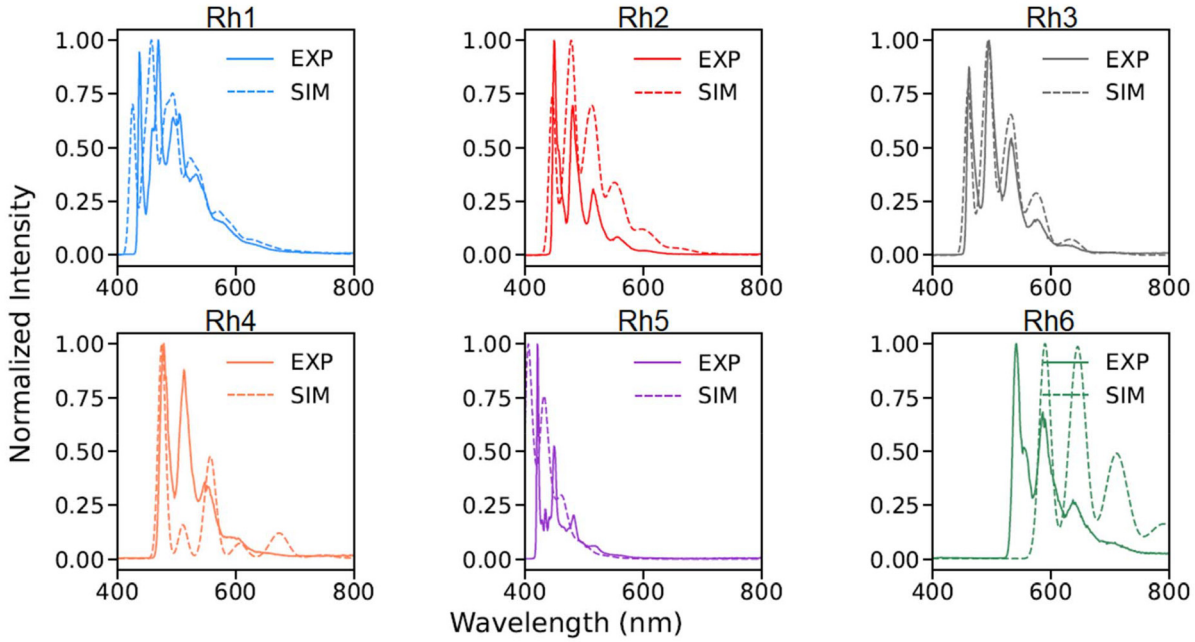

Fig. 3 Experimental (77K, solid line) and simulated (dashed line) emission spectra of the $[Rh(dfppz)_2(N^N)]^+$ complexes.

ones (Fig. 3). In analogy with the previously reported $[Rh(ppz)_2(N^N)]^+$ complexes,[37] the lowest excited states of nearly all complexes investigated here exhibit predominant LC character, localized mainly on the N^N ligand.

The situation is slightly different in the case of the $[Rh(dfppz)_2(dpq)]^+$ complex. The analysis of the computed spin density redistribution within its excited $^{3*}[Rh(dfppz)_2(dpq)]^+$ triplet state indicates the MLCT nature, similar to that observed for the non-fluorinated $[Rh(dfppz)_2(dpq)]^+$ analogue. Due to the hindered solvent relaxation, the energy of the ^{3*}MLCT state at 77 K is higher than the energy of the excited state localized on the dpq ligand of the $[Rh(dfppz)_2(dpq)]^+$ complex and therefore LC emission is observed under these experimental conditions, similar to that observed for the other complexes.

At room temperature, weak emission is observed only for the $[Rh(dfppz)_2(dppz)]^+$ complex (footnotes below Table 3). In MeCN solution at 298 K, this cation exhibits a structured emission band, red-shifted by a few nanometers relative to the band observed at 77 K (Fig. S16). The measured emission quantum yield of this complex (λ_{em} = 0.21%) is approximately twice that of the $[Rh(ppz)_2(dppz)]^+$ analogue (λ_{em} = 0.13%) but still is very low.[37] Considering the spectral structure, emission wavelength, and very low quantum yield, this band can be tentatively assigned to a ^{3*}LC transition localized on the dppz ligand. The remaining complexes studied are almost non-emitting in MeCN solution at 298 K. This is a consequence of the presence of an additional, thermally activated deactivation channel associated with a relatively low-lying excited ^{3*}MC state and the higher energy of the ^{3*}MLCT state. This makes the $S_0 \leftarrow {}^{3*}MC \leftarrow {}^{3*}MLCT$ deactivation channel operative under this temperature regime.[24,37,41,47]

Table 3 The Stern–Volmer quenching constant for the investigated $[Rh(dfppz)_2(N^N)](PF_6)$ complexes

Complex	$K_{SV\ DNA}$ [M^{-1}]
$[Rh(dfppz)_2(bpy)](PF_6)$	2.38×10^4
$[Rh(dfppz)_2(phen)](PF_6)$	1.74×10^4
$[Rh(dfppz)_2(tmphen)](PF_6)$	2.40×10^4
$[Rh(dfppz)_2(dpphen)](PF_6)$	2.81×10^4
$[Rh(dfppz)_2(dpq)](PF_6)$	2.96×10^4
$[Rh(dfppz)_2(dppz)](PF_6)$	4.83×10^4

Ethidium bromide (EB) displacement studies

The preliminary DNA-binding properties of the studied rhodium(III) complexes were evaluated using emission titrations. The fluorescence spectra of EB bound to CT-DNA in the absence and presence of these $[Rh(dfppz)_2(N^N)](PF_6)$ complexes are depicted in Fig. 4 and S24 (*cf.* the SI). Increasing the concentration of the complexes led to hypochromism, suggesting that the complexes can replace the EB molecules and bind with DNA through an intercalation mode, which suggests potential antitumor activities. However, further biological assays are required to evaluate the cytotoxic properties of these promising compounds.

The Stern–Volmer constants (K_{SV}) for the studied complexes are presented in Table 3 and follow the order **Rh2** < **Rh1** ≈ **Rh3** < **Rh4** < **Rh5** < **Rh6**. The intercalative interaction of **Rh6** with CT-DNA is the strongest in this series. It is evident that the principal factor influencing the intercalating properties of these complexes is the extension of the aromatic system of the N^N ligand. The quenching constants determined for the **Rh5** and **Rh6** complexes are approximately twice and three times

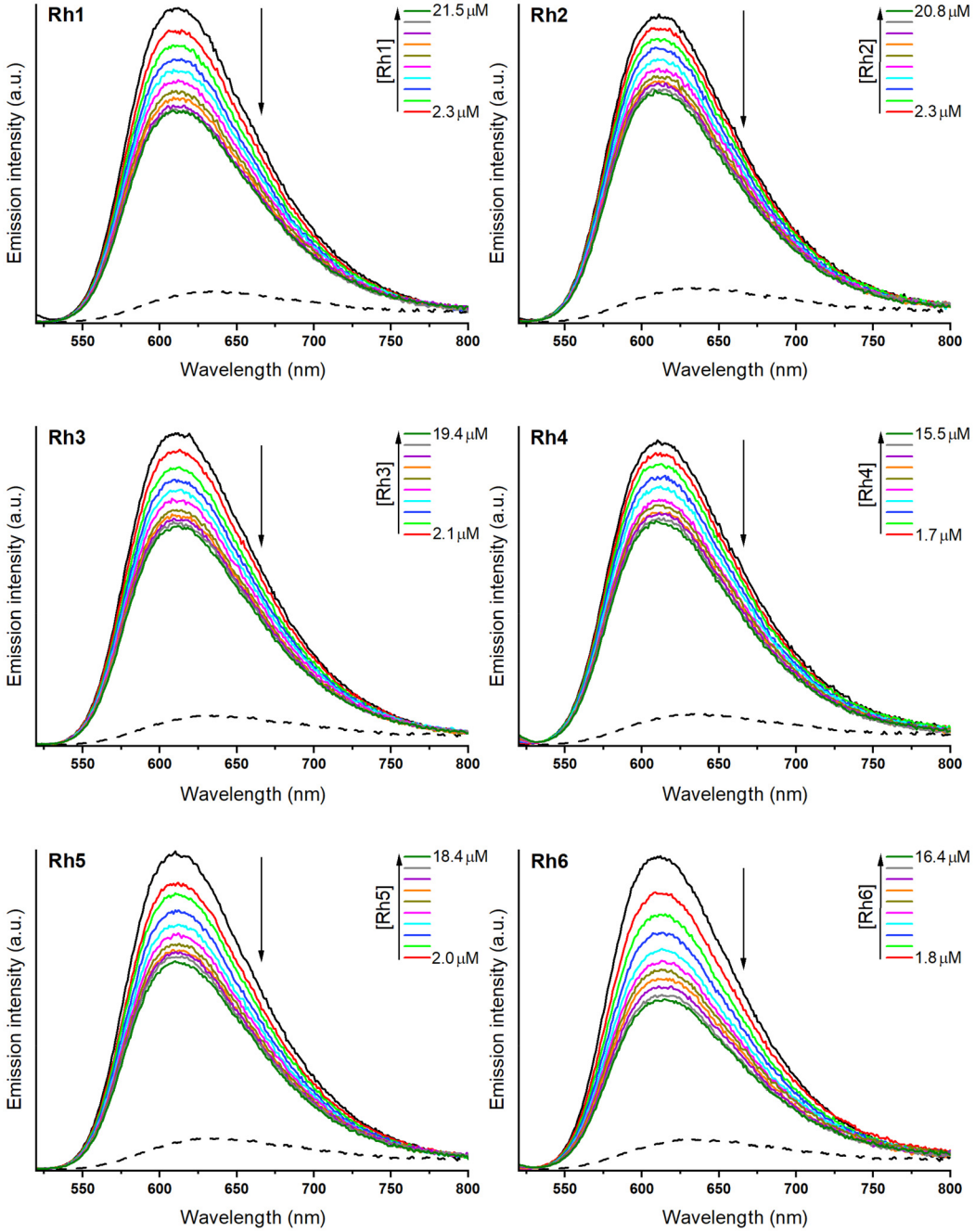

Fig. 4 Fluorescence emission spectra (λ_{ex} = 510 nm) of EB (black dotted line), the stock solution of EB–CT-DNA (black solid line), and the studied [Rh(dfppz)$_2$(N^N)](PF$_6$) complexes with increasing amounts of ~2–20 μM (other lines). [EB] = 5 μM and [CT-DNA] = 100 μM. The arrows indicate changes in the emission intensity upon aliquot addition of the studied complex solutions.

higher, respectively, than that of the **Rh2** complex (Table 3 and Fig. 5).

The different DNA-binding behaviours of these complexes are also consistent with our DFT computations. The π–π stacking interactions play an important role when complexes intercalate (or partially intercalate) into DNA,[48] and theoretical studies show that the DNA molecule acts as an electron donor while the intercalative complex as an electron acceptor.[49,50]

Among the group of complexes studied, those containing dpq and dppz as auxiliary ligands show the greatest tendency for π–π stacking interactions (Fig. 5). Therefore, factors affecting DNA-binding affinities can be considered in terms of the planarity and plane area of the intercalative ligand, and the energy and electron population of the lowest unoccupied molecular orbital (LUMO). A lower LUMO energy facilitates electron acceptance from the HOMO of DNA base pairs, while

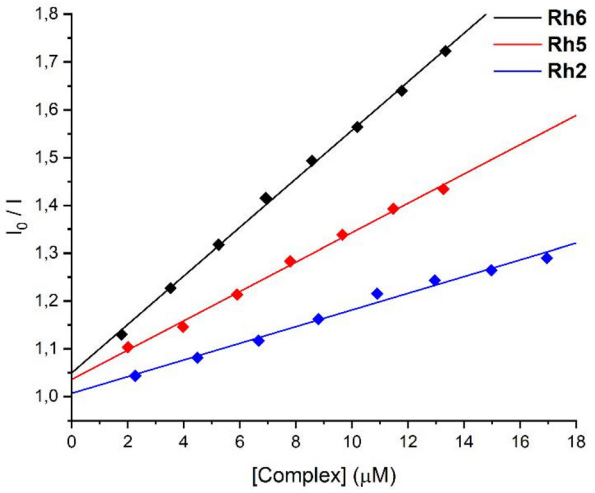

Fig. 5 Stern–Volmer plots of appropriate complex–EB–CT-DNA systems at room temperature; data for [Rh(dfppz)$_2$(phen)](PF$_6$), [Rh(dfppz)$_2$(dpq)](PF$_6$) and [Rh(dfppz)$_2$(dppz)](PF$_6$) are given.

greater LUMO electron density localized on the intercalative ligand enhances orbital overlap. In this series, the planar area of the intercalative ligand coordinated in the complex increases in the order phen < dpq < dppz, whereas the LUMO energies change in the opposite direction (*cf.* the SI). Moreover, the LUMO electron density is more strongly localized on the dppz ligand of **Rh6** than on the intercalative ligands of the other complexes. Thus, the experimental trend in the DNA-binding constants is fully supported by the theoretical results.

Conclusions

In summary, we prepared and characterized a new set of six cyclometallated rhodium(III) complexes of the type [Rh(dfppz)$_2$(N^N)](PF$_6$), incorporating fluorine-substituted cyclometallating ligands (dfppz) in combination with a family of α-diimine (N^N) ancillary ligands. A detailed comparison with their non-fluorinated analogues [Rh(ppz)$_2$(N^N)](PF$_6$) reveals that the introduction of fluorine substituents exerts a pronounced influence on spectroscopic and photophysical properties, while leaving the overall distorted octahedral coordination geometry essentially unchanged. The Rh–C$_{dfppz}$ bonds adopt a *cis*-orientation as in the ppz analogues, and only subtle variations are observed in the Rh–N$_{N^N}$ bond distances. In the NMR spectra, characteristic upfield shifts of the signals of protons attached to the dfppz$^-$ carbon atoms adjacent to the fluorinated carbons, together with downfield shifts of the cyclometallating carbon and fluorine-substituted carbon signals, clearly reflect the electronic impact of fluorination.

The absorption spectra of the fluorinated and non-fluorinated classes of complexes are very similar, with only a modest hypsochromic shift of the highest-energy bands observed for the dfppz complexes. At 77 K, both families of complexes display nearly identical phosphorescence arising from intraligand transitions localized on the N^N ligands. However, fluorination significantly extends the phosphorescence lifetimes. At room temperature, the complexes are weakly emissive or non-emissive, a behaviour attributed to a thermally activated non-radiative pathway involving a low-lying ^{3*}MC state, giving rise to an operative ^{3*}MLCT → ^{3*}MC → S$_0$ deactivation channel.

Finally, ethidium bromide displacement assays confirm that the [Rh(dfppz)$_2$(N^N)](PF$_6$) complexes interact with CT-DNA, suggesting potential biological activity. In particular, complexes bearing extended aromatic diimine ligands, such as dpq and dppz, which combine favorable π–π stacking interactions with lower LUMO energies, exhibit the strongest DNA-binding affinity. Overall, this study highlights the fluorination of cyclometallating ligands as an effective strategy for modulating the excited-state dynamics, emission lifetimes, and DNA-interaction profiles of Rh(III) complexes. These insights may serve as a useful platform for the rational design of new photoactive and bioactive organometallic systems.

Experimental

Materials

Unless otherwise stated, rhodium(III) chloride, α-diimines (bpy, phen, tmphen, dpphen, and dpq), and other required chemicals were purchased from Sigma-Aldrich, Alfa Aesar, or Trimen and used as received without further purification in the syntheses and purification of the investigated complexes. The dppz ligand was prepared according to the reported procedure.[51] The Hdfppz cyclometallating ligand was obtained following a literature method.[52] The dichloro-bridged [(dfppz)$_2$Rh-μ-Cl]$_2$ complex was synthesized as described previously.[41] Solvents for UV-vis absorption and emission studies (acetonitrile, methanol, and ethanol; Uvasol®, spectroscopic grade) were purchased from Merck.

Spectroscopy and spectrometry

^{1}H, ^{13}C, ^{31}P and ^{19}F NMR spectra were recorded using a Varian 400-MR spectrometer. Elemental analyses (C, H, and N) were carried out using an Elementar Vario Micro Cube analyzer. ESI-MS spectra of complexes (CH$_3$CN solution) were obtained using a micrOTOF-Q II (Bruker Daltonics). UV-vis absorption spectra were obtained with a Shimadzu UV-3100 spectrometer in the range of 200–600 nm using spectroscopic-grade solvents (acetonitrile and MeOH/EtOH, 1 : 1 v/v). Corrected steady-state emission spectra were recorded using a Gilden Photonics FluoroSense fluorimeter. For emission studies at 298 K, solutions of the complexes in acetonitrile (ACN) were placed in 1 cm fluorimeter quartz cuvettes and carefully deaerated before measurement by prolonged saturation with preliminarily purified and dried argon. The emission quantum yield ϕ_{em} values (with an estimated error of *ca.* ±10%) were determined in relation to a solution of quinine sulphate in 0.1 N H$_2$SO$_4$, served as a reference luminophore with ϕ_{em} = 0.51.[53] Low-

temperature (77 K) measurements were performed in fused silica "NMR-type" tubes (3 mm i.d.), which were placed in a liquid-nitrogen Dewar flask equipped with a transparent bottom window. Emission decay times were recorded using a FluoroSense-P fluorimeter configured for time-resolved measurements in the microsecond range (temporal resolution: 0.01 μs). For lifetime experiments, the samples were excited at 350 nm, and the emission was monitored at the maxima of the corresponding steady-state spectra. The experimental decay curves were analysed by the single-curve method using the reference convolution based on the Marquardt algorithm[54] with χ^2 values, the distributions of residuals and the adjusted coefficients of determined R^2 values serving as the criteria in the evaluation of the fit quality. Lifetime τ_{em} values were determined with an estimated error of *ca.* ±10%.

Computational details

All the computations were performed using the Gaussian 16 package[55] using the B3PW91 functional[56–58] in conjunction with the LANL2DZ basis set, which includes a pseudopotential to describe core electrons for large atoms, augmented by polarization functions on all atoms except hydrogen atoms.[58–61] This setup is known to provide accurate results concerning the luminescence and excited properties from the excited states for transition metal complexes. Relativistic effects have not been explicitly taken into account. The solvent effects (CH_2Cl_2) have been modelled using the PCM[62] solvation regime within the UAKS topological model. All the ground and excited state structures were optimized and checked to be at a true minimum on the potential energy surface by diagonalizing the Hessian matrix (no imaginary frequency). The emission spectra were simulated with time-dependent DFT (TDDFT) methodology. Triplet excited state structures were relaxed using the unrestricted method. Post-treatment processes were performed using Gaussview and VMS[63] software packages (luminescence spectral analysis). Luminescence spectra and band assignment were processed using in-house Python programs https://github.com/Cam-Zedd/gausssian-script.

X-ray structure determination

The X-ray diffraction data were collected from single crystals at room temperature using a Bruker D8 FIXED-CHI diffractometer with a microfocus sealed tube, a multilayer mirror as a monochromator, and a Photon II 7 CPAD detector. All data were integrated with SAINT V8.41.[64] The diffractometer was equipped with an Oxford Cryostream low-temperature device and a Mo Kα radiation source (λ = 0.71073 Å) was used. A multi-scan absorption correction, using SADABS 2016/2, was applied.[65] The structures were solved by intrinsic phasing methods with SHELXT 2018/2 and refined by full-matrix least-squares methods against F^2 using SHELXL-2019/2.[66,67] All non-hydrogen atoms were refined with anisotropic displacement parameters. All hydrogen atoms were refined isotropically on calculated positions using a riding model with their U_{iso} values constrained to 1.5 times the U_{eq} values of their pivot atoms for terminal sp^3 carbon atoms and 1.2 times for all other carbon atoms. Crystallographic data for the structures reported in this paper have been deposited with the Cambridge Crystallographic Data Centre.[68] CCDC 2491211, 2491212, 2491213, 2491214 and 2491215 contain the supplementary crystallographic data for this paper.

DNA interaction studies

A protein-free solution of calf thymus DNA (CT-DNA) was prepared in Tris–HCl/NaCl buffer (pH ~7.2) and the concentration was measured from its absorption intensity at 260 nm using a molar absorption coefficient value of 6600 M^{-1} cm^{-1}. A solution of the complexes used in the experiments was also prepared in Tris–HCl buffer containing no more than 3% DMSO. The emission spectra of EB–DNA and the effect of addition of rhodium(III) complexes to the equilibrium of EB–DNA ([EB] = 5 μM, [CT-DNA] = 100 μM) were monitored. The concentration of the compounds analysed varied from 1.5 to 20 μM (due to its solubility). Ethidium bromide (EB) displacement experiments were performed by monitoring the changes in the fluorescence intensity at excitation and emission wavelengths (λ_{ex}: 510; λ_{em}: 613 nm) after aliquot addition of the studied complexes to an aqueous solution of EB–DNA. The quenching constants for the complexes were calculated using a literature method.[69]

Preparation of the $[Rh(dfppz)_2(N^N)](PF_6)$ complexes

A series of six $[Rh(dfppz)_2(N^N)](PF_6)$ complexes were synthesized under similar conditions. In a typical procedure, 84.7 mg (0.10 mmol) of the dinuclear precursor $[(dfppz)_2Rh\text{-}\mu\text{-}Cl]_2$ and the appropriate N^N ligand (2.1–2.5 equiv.) were refluxed with stirring under an inert atmosphere in 20–25 ml of dichloromethane for *ca.* 3–4 h. After the reaction was completed, the mixture was cooled to room temperature, and then 2 ml of 10% NH_4PF_6 solution in methanol was added. The solution was filtered to remove precipitated inorganic salts, and the product was then precipitated by addition of diethyl ether. The solid was collected by filtration, washed with diethyl ether, and dried. In order to obtain spectroscopically pure complexes suitable for photophysical studies, the resulting crude products were purified by column chromatography using silica gel 60 (63–200 μm mesh) with CH_2Cl_2 followed by mixtures of CH_2Cl_2/MeOH (100 : 1) and finally CH_2Cl_2/MeOH (100 : 2.5) as eluents. The isolated complexes were then recrystallized.

Rh1. Yield: 94%. ^{1}H NMR (400 MHz, CD_3CN, ppm): δ 8.51 (dt, J_{H-H} = 8.2, 1.0 Hz, 2H of bpy), 8.48 (d, J_{H-H} = 2.9 Hz, 2H of pyrazole ring), 8.21 (td, J_{H-H} = 7.9, 1.6 Hz, 2H of bpy), 8.15 (d, J_{H-H} = 5.3 Hz, 2H of bpy), 7.56 (ddd, J_{H-H} = 7.6, 5.4, 1.2 Hz, 2H of bpy), 7.06 (d, J_{H-H} = 2.4 Hz, 2H of pyrazole ring), 6.86 (ddd, J_{H-H} = 11.8, 9.0, 2.5 Hz, 2H of phenyl ring), 6.59 (t, J_{H-H} = 2.7 Hz, 2H of pyrazole ring), 5.77 (ddt, J_{H-H} = 7.9, 2.3, 1.1 Hz, 2H of phenyl ring), (18 protons). $^{13}C\{^1H\}$ NMR (400 MHz, CD_3CN, ppm): δ 160.52 (ddd, J_{C-F} = 251.1, 10.3, 3.1 Hz), 155.82 (s), 153.97 (ddd, J_{C-Rh} = 30.9 Hz, J_{C-F} = 5.4, 3.4 Hz), 152.18 (s), 150.27 (dd, J_{C-F} = 254.0, 12.2 Hz), 141.18 (s), 140.27 (s), 133.14 (d, J_{C-F} = 14.8 Hz), 128.72 (s), 127.53 (m), 125.08 (s), 116.63

(dd, J_{C-F} = 20.2, 3.4 Hz), 110.28 (d, J_{C-F} = 1.9 Hz), 101.31 (dd, J_{C-F} = 28.1, 23.8 Hz). ^{19}F NMR (400 MHz, CD_3CN, ppm): δ −72.96 (d, J = 706.1 Hz, 6F of PF_6^-), −113.62 (m, 2F of phenyl ring), −123.68 (dd, J = 12.2, 5.5 Hz, 2F of phenyl ring). ^{31}P NMR (400 MHz, CD_3CN, ppm): δ −144.66 (sep, J_{P-F} = 706.7 Hz, 1P). Anal. calc. (%) for $C_{28}H_{18}N_6F_{10}PRh$: C, 44.11; H, 2.38; N, 11.02. Found: C, 44.13; H, 2.57; N, 10.83. MS (ESI) m/z calculated for ($[M - PF_6^-]^+$) 617.0584, found 617.0585.

Rh2. Yield: 83%. ^{1}H NMR (400 MHz, CD_3CN, ppm): δ 8.76 (dd, J_{H-H} = 8.3, 1.5 Hz, 2H of phen), 8.48 (dd, J_{H-H} = 5.0, 1.4 Hz, 2H of phen), 8.46 (d, J_{H-H} = 3.0 Hz, 2H of pyrazole ring), 8.24 (s, 2H of phen), 7.88 (dd, J_{H-H} = 8.3, 5.0 Hz, 2H of phen), 6.92 (d, J_{H-H} = 2.2 Hz, 2H of pyrazole ring), 6.90 (ddd, J_{H-H} = 12.2, 9.0, 2.5 Hz, 2H of phenyl ring), 6.49 (t, J_{H-H} = 2.6 Hz, 2H of pyrazole ring), 5.88 (ddt, J_{H-H} = 8.0, 2.5, 1.2 Hz, 2H of phenyl ring), (18 protons). $^{13}C\{^1H\}$ NMR (400 MHz, CD_3CN, ppm): δ 160.51 (ddd, J_{C-F} = 250.9, 9.8, 2.4 Hz), 153.69 (ddd, J_{C-Rh} = 31.5 Hz, J_{C-F} = 5.5, 3.1 Hz), 152.65 (s), 150.28 (ddd, J_{C-F} = 254.2, 12.4, 1.4 Hz), 146.72 (s), 140.38 (s), 140.15 (s), 133.07 (d, J_{C-F} = 14.8 Hz), 132.04 (s), 128.90 (s), 127.73 (m), 127.19 (s), 116.79 (dd, J_{C-F} = 20.2, 3.1 Hz), 110.13 (d, J_{C-F} = 2.6 Hz), 101.36 (dd, J_{C-F} = 28.2, 23.9 Hz). ^{19}F NMR (400 MHz, CD_3CN, ppm): δ −72.94 (d, J = 706.1 Hz, 6F of PF_6^-), −113.71 (m, 2F of phenyl ring), −123.79 (dd, J = 12.2, 4.9 Hz, 2F of phenyl ring). ^{31}P NMR (400 MHz, CD_3CN, ppm): δ −144.66 (sep, J_{P-F} = 706.2 Hz, 1P). Anal. calc. (%) for $C_{30}H_{18}N_6F_{10}PRh$: C, 45.82; H, 2.31; N, 10.69. Found: C, 45.89; H, 2.59; N, 10.33. MS (ESI) m/z calculated for ($[M - PF_6^-]^+$) 641.0584, found 641.0585.

Rh3. Yield: 91%. ^{1}H NMR (400 MHz, CD_3CN, ppm): δ 8.46 (d, J_{H-H} = 2.9 Hz, 2H of pyrazole ring), 8.37 (s, 2H of tmphen), 8.17 (s, 2H of tmphen), 6.90 (d, J_{H-H} = 2.3 Hz, 2H of pyrazole ring), 6.87 (ddd, J_{H-H} = 12.0, 9.0, 2.5 Hz, 2H of phenyl ring), 6.49 (t, J_{H-H} = 2.7 Hz, 2H of pyrazole ring), 5.85 (ddt, J_{H-H} = 8.0, 2.5, 1.2 Hz, 2H of phenyl ring), 2.80 (s, 6H of tmphen), 2.42 (s, 6H of tmphen), (26 protons). $^{13}C\{^1H\}$ NMR (400 MHz, CD_3CN, ppm): δ 160.51 (ddd, J_{C-F} = 250.9, 10.0, 2.6 Hz), 154.55 (ddd, J_{C-Rh} = 31.0 Hz, J_{C-F} = 5.1, 3.3 Hz), 152.90 (s), 150.30 (ddd, J_{C-F} = 253.7, 12.5, 1.2 Hz), 147.90 (s), 145.36 (s), 140.06 (s), 135.88(s), 132.95 (d, J_{C-F} = 14.9 Hz), 130.33 (s), 127.70 (m), 124.88 (s), 116.75 (dd, J_{C-F} = 20.1, 3.1 Hz), 110.02 (d, J_{C-F} = 2.7 Hz), 101.19 (dd, J_{C-F} = 28.1, 23.8 Hz), 17.96 (CH_3 of tmphen), 15.33 (CH_3 of tmphen). ^{19}F NMR (400 MHz, CD_3CN, ppm): δ −72.97 (d, J = 706.3 Hz, 6F of PF_6^-), −113.78 (m, 2F of phenyl ring), −123.85 (dd, J = 12.1, 5.2 Hz, 2F of phenyl ring). ^{31}P NMR (400 MHz, CD_3CN, ppm): δ −144.68 (sep, J_{P-F} = 705.6 Hz, 1P). Anal. calc. (%) for $C_{34}H_{26}N_6F_{10}PRh$: C, 48.47; H, 3.11; N, 9.97. Found: C, 48.14; H, 3.04; N, 9.66. MS (ESI) m/z calculated for ($[M - PF_6^-]^+$) 697.1210, found 697.1212.

Rh4. Yield: 89%. ^{1}H NMR (400 MHz, CD_3CN, ppm): δ 8.53 (d, J_{H-H} = 5.2 Hz, 2H of dpphen), 8.51 (d, J_{H-H} = 2.9 Hz, 2H of pyrazole ring), 8.14 (s, 2H of dpphen), 7.82 (d, J_{H-H} = 5.2 Hz, 2H of dpphen), 7.70–7.58 (m, 10H of dpphen), 7.08 (d, J_{H-H} = 2.4 Hz, 2H of pyrazole ring), 6.92 (ddd, J_{H-H} = 12.0, 9.0, 2.5 Hz, 2H of phenyl ring), 6.56 (t, J_{H-H} = 2.7 Hz,2H of pyrazole ring), 5.92 (ddt, J_{H-H} = 7.9, 2.5, 1.2 Hz, 2H of phenyl ring) (26 protons). $^{13}C\{^1H\}$ NMR (400 MHz, CD_3CN, ppm): δ 160.61 (ddd, J_{C-F} = 251.4, 9.9, 2.5 Hz), 154.12 (ddd, J_{C-Rh} = 31.2 Hz, J_{C-F} = 5.3, 3.3 Hz), 152.45 (s), 152.14 (s), 150.34 (ddd, J_{C-F} = 254.2, 12.5, 1.2 Hz), 147.38 (s), 140.39 (s), 136.82 (s), 133.13 (d, J_{C-F} = 14.9 Hz), 130.74 (s), 130.71 (s), 130.12 (s), 129.97 (s), 127.75 (m), 127.38 (s), 126.76 (s), 116.83 (dd, J_{C-F} = 20.1, 3.1 Hz), 110.25 (d, J_{C-F} = 2.6 Hz), 101.40 (dd, J_{C-F} = 28.1, 23.8 Hz). ^{19}F NMR (400 MHz, CD_3CN, ppm): δ −72.96 (d, J = 706.1 Hz, 6F of PF_6^-), −113.61 (m, 2F of phenyl ring), −123.72 (dd, J = 12.2, 5.3 Hz, 2F of phenyl ring). ^{31}P NMR (400 MHz, CD_3CN, ppm): δ −144.67 (sep, J_{P-F} = 706.7 Hz, 1P). Anal. calc. (%) for $C_{42}H_{26}N_6F_{10}PRh$: C, 53.75; H, 2.79; N, 8.95. Found: C, 53.47; H, 2.87; N, 8.79. MS (ESI) m/z calculated for ($[M - PF_6^-]^+$) 793.1210, found 793.1210.

Rh5. Yield: 86%. ^{1}H NMR (400 MHz, CD_3CN, ppm): δ 9.73 (dd, J_{H-H} = 8.3, 1.5 Hz, 2H of dpq), 9.22 (s, 2H of dpq), 8.58 (dd, J_{H-H} = 5.0, 1.5, Hz, 2H of dpq), 8.49 (d, J_{H-H} = 2.9 Hz, 2H of pyrazole ring), 8.03 (dd, J_{H-H} = 8.3, 5.0 Hz, 2H of dpq), 7.02 (d, J_{H-H} = 2.4 Hz, 2H of pyrazole ring), 6.92 (ddd, J_{H-H} = 12.0, 9.0, 2.5 Hz, 2H of phenyl ring), 6.52 (t, J_{H-H} = 2.6 Hz,2H of pyrazole ring), 5.89 (ddt, J_{H-H} = 8.0, 2.5, 1.2 Hz, 2H of phenyl ring) (18 protons). $^{13}C\{^1H\}$ NMR (400 MHz, CD_3CN, ppm): δ 160.54 (ddd, J_{C-F} = 251.1, 10.1, 2.5 Hz), 154.02 (s), 153.32 (ddd, J_{C-Rh} = 31.4 Hz, J_{C-F} = 5.3, 3.0 Hz), 150.33 (ddd, J_{C-F} = 254.3, 12.3, 1.2 Hz), 148.32 (s), 147.71 (s), 140.61 (s), 140.59 (s), 136.70 (s), 133.20 (d, J_{C-F} = 14.8 Hz), 131.05 (s), 128.30 (s), 127.75 (m), 116.81 (dd, J_{C-F} = 20.2, 3.1 Hz), 110.16 (d, J_{C-F} = 1.9 Hz), 101.48 (dd, J_{C-F} = 28.3, 23.8 Hz). ^{19}F NMR (400 MHz, CD_3CN, ppm): δ −72.97 (d, J = 706.9 Hz, 6F of PF_6^-), −113.57 (m, 2F of phenyl ring), −123.63 (dd, J = 12.2, 5.3 Hz, 2F of phenyl ring). ^{31}P NMR (400 MHz, CD_3CN, ppm): δ −144.66 (sep, J_{P-F} = 705.8 Hz, 1P). Anal. calc. (%) for $C_{32}H_{18}N_8F_{10}PRh$: C, 45.84; H, 2.16; N, 13.37. Found: C, 46.04; H, 2.03; N, 13.45. MS (ESI) m/z calculated for ($[M - PF_6^-]^+$) 693.0646, found 693.0646.

Rh6. Yield: 77%. ^{1}H NMR (400 MHz, CD_3CN, ppm): δ 9.82 (dd, J_{H-H} = 8.3, 1.5 Hz, 2H of dppz), 8.57 (dd, J_{H-H} = 5.1, 1.5 Hz, 2H of dppz), 8.51 (d, J_{H-H} = 2.9 Hz, 2H of pyrazole ring), 8.45 (dd, J_{H-H} = 6.6, 3.4 Hz, 2H of dppz), 8.12 (dd, J_{H-H} = 6.6, 3.4 Hz, 2H of dppz), 8.03 (dd, J_{H-H} = 8.3, 5.1 Hz, 2H of dppz), 7.10 (d, J_{H-H} = 2.4 Hz, 2H of pyrazole ring), 6.93 (ddd, J_{H-H} = 12.1, 9.0, 2.5 Hz, 2H of phenyl ring), 6.54 (t, J_{H-H} = 2.6 Hz, 2H of pyrazole ring), 5.90 (ddt, J_{H-H} = 7.9, 2.5, 1.2 Hz, 2H of phenyl ring) (20 protons). $^{13}C\{^1H\}$ NMR (400 MHz, CD_3CN, ppm): δ 160.56 (ddd, J_{C-F} = 251.1, 10.0, 2.5 Hz), 154.08 (s), 153.30 (ddd, J_{C-Rh} = 31.3 Hz, J_{C-F} = 5.2, 2.9 Hz), 150.25 (ddd, J_{C-F} = 254.3, 12.5, 1.1 Hz), 149.47 (s), 143.73 (s), 140.85 (s), 140.61 (s), 136.93 (s), 133.47 (s), 133.25 (d, J_{C-F} = 15.0 Hz), 131.66 (s), 130.60 (s), 128.62 (s), 127.74 (m), 116.81 (dd, J_{C-F} = 20.3, 3.2 Hz), 110.21 (d, J_{C-F} = 2.6 Hz), 101.50 (dd, J_{C-F} = 28.2, 23.8 Hz). ^{19}F NMR (400 MHz, CD_3CN, ppm): δ −72.96 (d, J = 706.1 Hz, 6F of PF_6^-), −113.51 (m, 2F of phenyl ring), −123.58 (dd, J = 12.1, 5.5 Hz, 2F of phenyl ring). ^{31}P NMR (400 MHz, CD_3CN, ppm): δ −144.67 (sep, J_{P-F} = 706.5 Hz, 1P). Anal. calc. (%) for $C_{36}H_{20}N_8F_{10}PRh$: C, 48.67; H, 2.27; N, 12.61. Found: C, 48.86; H, 2.21; N, 12.35. MS (ESI) m/z calculated for ($[M - PF_6^-]^+$) 743.0802, found 743.0804.

Author contributions

P. W.: methodology, investigation, data curation, and visualization. C. L.: methodology, formal analysis, investigation, data curation, visualization, and writing – review & editing. K. S.: methodology, formal analysis, investigation, data curation, validation, and writing – review & editing. A. K.: conceptualization, methodology, validation, formal analysis, investigation, resources, data curation, writing – original draft, writing – review & editing, and visualization. J. M.: investigation and data curation. M. U.: investigation and data curation.

Conflicts of interest

There are no conflicts to declare.

Data availability

All experimental and computational data supporting the findings of this study are included in the article and its supplementary information (SI). Supplementary information: ^{1}H, ^{13}C, ^{31}P and ^{19}F NMR spectra of the $[Rh(dfppz)_2(N^N)](PF_6)$ complexes, ESI-MS spectra, crystallographic data and refinement parameters, theoretical results and crystallographic data in CIF file for the $[Rh(dfppz)_2(N^N)](PF_6)$ complexes. See DOI: https://doi.org/10.1039/d5dt02369f.

Additional raw data or input/output files from quantum chemical calculations are available from the corresponding author upon reasonable request.

CCDC 2491211–2491215 contain the supplementary crystallographic data for this paper.[70a–e]

Acknowledgements

C. L. thanks the IUF for its support and the CCIPL for computational facilities.

References

1 T. Piou and T. Rovis, *Acc. Chem. Res.*, 2018, **51**, 170–180.
2 C.-H. Leung, H.-J. Zhong, D. S.-H. Chan and D.-L. Ma, *Coord. Chem. Rev.*, 2013, **257**, 1764–1776.
3 D.-L. Ma, M. Wang, Z. Mao, C. Yang, C.-T. Ng and C.-H. Leung, *Dalton Trans.*, 2016, **45**, 2762–2771.
4 M. Sohrabi, M. Bikhof Torbati, M. Lutz, S. Meghdadi, H. Farrokhpour, A. Amiri and M. Amirnasr, *J. Photochem. Photobiol., A*, 2022, **423**, 113573.
5 W. Xiang, S. He, T. Kuang, J. Yin, B. Hu, C. Sun, J. He, J. Wang, C.-Y. Yu and H. Wei, *Mater. Today Bio*, 2025, **33**, 101941.
6 S. Saha, R. Kushwaha, A. Mandal, N. Singh and S. Banerjee, *Coord. Chem. Rev.*, 2025, **525**, 216306.
7 U. Das, B. Kar, S. Pete and P. Paira, *Dalton Trans.*, 2021, **50**, 11259–11290.
8 Y. Geldmacher, M. Oleszak and W. S. Sheldrick, *Inorg. Chim. Acta*, 2012, **393**, 84–102.
9 S. Mukhopadhyay, R. K. Gupta, R. P. Paitandi, N. K. Rana, G. Sharma, B. Koch, L. K. Rana, M. S. Hundal and D. S. Pandey, *Organometallics*, 2015, **34**, 4491–4506.
10 H. Liang, T. Hao, C. Yin, X. Yang, H. Fu, X. Zheng, R. Li, D. Xiao and H. Chen, *Eur. J. Inorg. Chem.*, 2017, **2017**, 4149–4157.
11 P. A. Vekariya, P. S. Karia, J. V. Vaghasiya, S. Soni, E. Suresh and M. N. Patel, *Polyhedron*, 2016, **110**, 73–84.
12 J. D. Knoll and C. Turro, *Coord. Chem. Rev.*, 2015, **282–283**, 110–126.
13 R. Esteghamat-Panah, H. Hadadzadeh, H. Farrokhpour, J. Simpson, A. Abdolmaleki and F. Abyar, *Eur. J. Med. Chem.*, 2017, **127**, 958–971.
14 H. A. Sahyon, F. Althobaiti, A. E.-M. M. Ramadan and A. M. Fathy, *J. Mol. Struct.*, 2022, **1257**, 132584.
15 B. M. Zeglis, V. C. Pierre and J. K. Barton, *Chem. Commun.*, 2007, **7345**, 4565.
16 M. A. Scharwitz, I. Ott, Y. Geldmacher, R. Gust and W. S. Sheldrick, *J. Organomet. Chem.*, 2008, **693**, 2299–2309.
17 Y. Geldmacher, R. Rubbiani, P. Wefelmeier, A. Prokop, I. Ott and W. S. Sheldrick, *J. Organomet. Chem.*, 2011, **696**, 1023–1031.
18 S. DiLuzio, V. Mdluli, T. U. Connell, J. Lewis, V. VanBenschoten and S. Bernhard, *J. Am. Chem. Soc.*, 2021, **143**, 1179–1194.
19 S. DiLuzio, M. Baumer, R. Guzman, H. Kagalwala, E. Lopato, S. Talledo, J. Kangas and S. Bernhard, *Inorg. Chem.*, 2024, **63**, 14267–14277.
20 K. K.-W. Lo, C.-K. Li, K.-W. Lau and N. Zhu, *Dalton Trans.*, 2003, **3**, 4682.
21 F. Wei, S. Lai, S. Zhao, M. Ng, M. Chan, V. W. Yam and K. M. Wong, *J. Am. Chem. Soc.*, 2019, **141**, 12863–12871.
22 S. Pal, S. Joy, H. Paul, S. Banerjee, A. Maji, E. Zangrando and P. Chattopadhyay, *J. Phys. Chem. C*, 2017, **121**, 11632–11642.
23 Y. Ohsawa, S. Sprouse, K. A. King, M. K. DeArmond, K. W. Hanck and R. J. Watts, *J. Phys. Chem.*, 1987, **91**, 1047–1054.
24 M. Maestri, D. Sandrini, V. Balzani, U. Maeder and A. Von Zalewsky, *Inorg. Chem.*, 1987, **26**, 1323–1327.
25 D. Sandrini, M. Maestri, V. Balzani, U. Maeder and A. von Zelewsky, *Inorg. Chem.*, 1988, **27**, 2640–2643.
26 D. Sandrini, M. Maestri, M. Ciano, U. Maeder and A. von Zelewsky, *Helv. Chim. Acta*, 1990, **73**, 1306–1313.
27 E. V. Ivanova, M. V. Puzyk and K. P. Balashev, *Opt. Spectrosc.*, 2009, **107**, 101–105.
28 M. Graf, Y. Gothe, N. Metzler-Nolte, R. Czerwieniec and K. Sünkel, *J. Organomet. Chem.*, 2014, **765**, 46–52.
29 M. Graf, Y. Gothe, N. Metzler-nolte, R. Czerwieniec and K. Sünkel, *Inorg. Chim. Acta*, 2017, **463**, 36–43.
30 Y. Chen, C. Liu and L. Wang, *Tetrahedron*, 2019, **75**, 130686.

31 Y. Yang, L. Guo, X. Ge, T. Zhu, W. Chen, H. Zhou, L. Zhao and Z. Liu, *Inorg. Chem.*, 2020, **59**, 748–758.
32 M. Naoui, H. Brahim and A. Guendouzi, *J. Photochem. Photobiol., A*, 2020, 112624.
33 J. C. Páez-Franco, M. R. Zermeño-Ortega, C. M. de la O-Contreras, D. Canseco-González, J. R. Parra-Unda, A. Avila-Sorrosa, R. G. Enríquez, J. M. Germán-Acacio and D. Morales-Morales, *Pharmaceutics*, 2022, **14**, 402.
34 M. Crespo, *Organometallics*, 2012, **31**, 1216–1234.
35 A. Kamecka, A. Kapturkiewicz and Ł. Pipczyński, *Inorg. Chem. Commun.*, 2021, **131**, 108764.
36 A. Kapturkiewicz and A. Kamecka, *RSC Adv.*, 2021, **11**, 29308–29322.
37 A. Kamecka, A. Kapturkiewicz, P. Wójcik, K. Suwińska, J. Masternak and N. Barbarczyk, *Struct. Chem.*, 2025, **36**, 709–722.
38 A. Kamecka, A. Kapturkiewicz, P. Wójcik, K. Suwińska and J. Masternak, *Eur. J. Inorg. Chem.*, 2023, **202300438**, 1–11.
39 M. Nonoyama, *J. Organomet. Chem.*, 1975, **86**, 263–267.
40 P. J. Steel, *J. Organomet. Chem.*, 1991, **408**, 395–402.
41 P. Wójcik, C. Latouche, K. Suwińska and A. Kamecka, *Dalton Trans.*, 2025, **54**, 12018–12029.
42 A. L. de Oliveira, C. H. Alves de Oliveira, L. M. Mairink, F. Pazini, R. Menegatti and L. M. Lião, *Magn. Reson. Chem.*, 2011, **49**, 537–542.
43 A. B. Tamayo, B. D. Alleyne, P. I. Djurovich, S. Lamansky, I. Tsyba, N. N. Ho, R. Bau and M. E. Thompson, *J. Am. Chem. Soc.*, 2003, **125**, 7377–7387.
44 G. Frei, A. Zilian, A. Raselli, H. U. Guedel and H. B. Buergi, *Inorg. Chem.*, 1992, **31**, 4766–4773.
45 Y. Komada, S. Yamauchi and N. Hirota, *J. Phys. Chem.*, 1986, **90**, 6425–6430.
46 E. L. Menon, R. Perera, M. Navarro, R. J. Kuhn and H. Morrison, *Inorg. Chem.*, 2004, **43**, 5373–5381.
47 I. B. Losada and P. Persson, *Chem. Sci.*, 2023, **14**, 13713–13721.
48 X.-H. Zou, B.-H. Ye, H. Li, Q.-L. Zhang, H. Chao, J.-G. Liu, L.-N. Ji and X.-Y. Li, *JBIC, J. Biol. Inorg. Chem.*, 2001, **6**, 143–150.
49 L.-M. Chen, J. Liu, J.-C. Chen, C.-P. Tan, S. Shi, K.-C. Zheng and L.-N. Ji, *J. Inorg. Biochem.*, 2008, **102**, 330–341.
50 Y.-M. Chen, A.-G. Zhang, Y.-J. Liu and K.-Z. Wang, *J. Organomet. Chem.*, 2011, **696**, 1716–1722.
51 J. Dickeson and L. Summers, *Aust. J. Chem.*, 1970, **23**, 1023.
52 L. He, L. Duan, J. Qiao, G. Dong, L. Wang and Y. Qiu, *Chem. Mater.*, 2010, **22**, 3535–3542.
53 R. A. Velapoldi and H. H. Tønnesen, *J. Fluoresc.*, 2004, **14**, 465–472.
54 D. W. Marquardt, *J. Soc. Ind. Appl. Math.*, 1963, **11**, 431–441.
55 M. J. Frisch, G. W. Trucks, H. B. Schlegel, G. E. Scuseria, M. A. Robb, J. R. Cheeseman, G. Scalmani, V. Barone, G. A. Petersson, H. Nakatsuji, X. Li, M. Caricato, A. V. Marenich, J. Bloino, B. G. Janesko, R. Gomperts, B. Mennucci, H. P. Hratchian, J. V. Ortiz, A. F. Izmaylov, J. L. Sonnenberg, D. Williams-Young, F. Ding, F. Lipparini, F. Egidi, J. Goings, B. Peng, A. Petrone, T. Henderson, D. Ranasinghe, V. G. Zakrzewski, J. Gao, N. Rega, G. Zheng, W. Liang, M. Hada, M. Ehara, K. Toyota, R. Fukuda, J. Hasegawa, M. Ishida, T. Nakajima, Y. Honda, O. Kitao, H. Nakai, T. Vreven, K. Throssell, J. A. Montgomery Jr., J. E. Peralta, F. Ogliaro, M. J. Bearpark, J. J. Heyd, E. N. Brothers, K. N. Kudin, V. N. Staroverov, T. A. Keith, R. Kobayashi, J. Normand, K. Raghavachari, A. P. Rendell, J. C. Burant, S. S. Iyengar, J. Tomasi, M. Cossi, J. M. Millam, M. Klene, C. Adamo, R. Cammi, J. W. Ochterski, R. L. Martin, K. Morokuma, O. Farkas, J. B. Foresman and D. J. Fox, *Gaussian 16, Revision C.01*, Gaussian, Inc., Wallingford, CT, 2016.
56 J. P. Perdew, *Phys. Rev. B: Condens. Matter Mater. Phys.*, 1986, **33**, 8822–8824.
57 A. D. Becke, *J. Chem. Phys.*, 1993, **98**, 5648–5652.
58 R. Schira and C. Latouche, *Dalton Trans.*, 2021, **50**, 746–753.
59 W. R. Wadt and P. J. Hay, *J. Chem. Phys.*, 1985, **82**, 284–298.
60 P. J. Hay and W. R. Wadt, *J. Chem. Phys.*, 1985, **82**, 270–283.
61 P. J. Hay and W. R. Wadt, *J. Chem. Phys.*, 1985, **82**, 299–310.
62 B. Mennucci, J. Tomasi, R. Cammi, J. R. Cheeseman, M. J. Frisch, F. J. Devlin, S. Gabriel and P. J. Stephens, *J. Phys. Chem. A*, 2002, **106**, 6102–6113.
63 D. Licari, A. Baiardi, M. Biczysko, F. Egidi, C. Latouche and V. Barone, *J. Comput. Chem.*, 2015, **36**, 321–334.
64 *Bruker, SAINT, V8.41*, Bruker AXS Inc., Madison, Wisconsin, USA.
65 L. Krause, R. Herbst-Irmer, G. M. Sheldrick and D. Stalke, *J. Appl. Crystallogr.*, 2015, **48**, 3–10.
66 G. M. Sheldrick, *Acta Crystallogr., Sect. C: Struct. Chem.*, 2015, **71**, 3–8.
67 G. M. Sheldrick, *Acta Crystallogr., Sect. A: Found. Adv.*, 2015, **71**, 3–8.
68 C. R. Groom, I. J. Bruno, M. P. Lightfoot and S. C. Ward, *Acta Crystallogr., Sect. B:Struct. Sci., Cryst. Eng. Mater.*, 2016, **72**, 171–179.
69 R. K. Gupta, R. Pandey, G. Sharma, R. Prasad, B. Koch, S. Srikrishna, P.-Z. Li, Q. Xu and D. S. Pandey, *Inorg. Chem.*, 2013, **52**, 3687–3698.
70 (*a*) CCDC 2491211: Experimental Crystal Structure Determination, 2025, DOI: 10.5517/ccdc.csd.cc2pm9n9; (*b*) CCDC 2491212: Experimental Crystal Structure Determination, 2025, DOI: 10.5517/ccdc.csd.cc2pm9pb; (*c*) CCDC 2491213: Experimental Crystal Structure Determination, 2025, DOI: 10.5517/ccdc.csd.cc2pm9qc; (*d*) CCDC 2491214: Experimental Crystal Structure Determination, 2025, DOI: 10.5517/ccdc.csd.cc2pm9rd; (*e*) CCDC 2491215: Experimental Crystal Structure Determination, 2025, DOI: 10.5517/ccdc.csd.cc2pm9sf.